

A Bayesian spatial temporal mixtures approach to kinetic parametric images in dynamic positron emission tomography

W. Zhu^{*}, J. Ouyang[†], Y. Rakvongthai[‡]
N. J. Guehl, D. W. Wooten, G. El Fakhri, M. D. Normandin[§]
Y. Fan[¶]

June 11, 2018

Abstract

Purpose: Estimation of parametric maps is challenging for kinetic models in dynamic positron emission tomography. Since voxel kinetics tend to be spatially contiguous, the authors consider groups of homogeneous voxels together. The authors propose a novel algorithm to identify the groups and estimate kinetic parameters simultaneously. Uncertainty estimates for kinetic parameters are also obtained.

Methods: Mixture models were used to fit the time activity curves. In order to borrow information from spatially nearby voxels, the Potts

^{*}School of Mathematics and Statistics, UNSW Australia, Sydney 2052, Australia

[†]Center for Advanced Medical Imaging Sciences, Massachusetts General Hospital, Boston, MA 02114 and Department of Radiology, Harvard Medical School, Boston, MA 02115, USA

[‡]Department of Radiology, Faculty of Medicine, Chulalongkorn University, Bangkok 10330, Thailand

[§]Center for Advanced Medical Imaging Sciences, Massachusetts General Hospital, Boston, MA 02114 and Department of Radiology, Harvard Medical School, Boston, MA 02115, USA

[¶]School of Mathematics and Statistics, UNSW Australia, Sydney 2052, Australia

model was adopted. A spatial temporal model was built incorporating both spatial and temporal information in the data. Markov chain Monte Carlo was used to carry out parameter estimation. Evaluation and comparisons with existing methods were carried out on cardiac studies using both simulated data sets and a pig study data. One-compartment kinetic modelling was used, in which K_1 is the parameter of interest, providing a measure of local perfusion.

Results: Based on simulation experiments, the median standard deviation across all image voxels, of K_1 estimates were 0, 0.13, and 0.16 for the proposed spatial mixture models (SMMs), standard curve fitting and spatial K -means methods respectively. The corresponding median mean squared biases for K_1 were 0.04, 0.06 and 0.06 for abnormal region of interest(ROI); 0.03, 0.03 and 0.04 for normal ROI; and 0.007, 0.02 and 0.05 for the noise region.

Conclusions: SMM is a fully Bayesian algorithm which determines the optimal number of homogeneous voxel groups, voxel group membership, parameter estimation and parameter uncertainty estimation simultaneously. The voxel membership can also be used for classification purposes. By borrowing information from spatially nearby voxels, SMM substantially reduces the variability of parameter estimates. In some ROIs, SMM also reduces mean squared bias.

keywords PET image, kinetic model, myocardium, spatial mixture model, MCMC.

1 Introduction

Dynamic positron emission tomography (PET) can be used to measure tracer kinetics in vivo, from which physiological parameters, such as tissue perfusion, ligand receptor binding potential, and metabolic rate can be determined using compartmental modelling techniques.

Estimation of the kinetic parametric images can be extremely challenging, since the data are often very noisy. Most conventional methods either define a region of interest (ROI) and estimate parameters based on the averages [Lammertsma and Hume \(1996\)](#); [Slifstein et al. \(2008\)](#); [Nye et al. \(2008\)](#), or in a voxelwise fashion. The former requires the identification of ROI which itself is difficult. The latter fails to utilize information from nearby voxels, resulting in more noisy estimates. Estimations are typically

carried out using a minimum least-squares approach [Gunn *et al.* \(1997\)](#) or a basis function approach [Gunn *et al.* \(2002\)](#). Given low signal-to-noise ratio (SNR), particularly in voxelwise estimations, some external constraints are often necessary to stabilize parameter estimation. Smoothness regularization can be used [Kamasak *et al.* \(2005\)](#); [Huang and Zhou \(1998\)](#), constraining the parameters from nearby spatial locations to be more similar. Similarly, Tikhonov regularization [O'Sullivan and Saha \(1999\)](#) can be used to directly constrain parameter values to be within a certain range, so that estimates obtained are less sensitive to noise. To account for irregularities in the noise distribution, mixture models can be fitted to each voxel [Lin *et al.* \(2014\)](#). In this case, it is necessary to restrict the total number of mixture components to be small and employ regularization to constrain parameter estimates.

Assuming a Gaussian error distribution, Bayesian methods [Zhou, Aston, and Johansen \(2013\)](#) provide an alternative way of obtaining uncertainty estimates for the kinetic parameters, as well as model choice for the competing compartmental models. However, these methods yield higher voxel to voxel variability because each voxel was processed independently, and the assumption of Gaussian distribution can also be inappropriate, leading to biased parameter estimates. This has led to the development of several approaches, in which a clustering method was performed first to cluster the PET images into several homogeneous regions, and kinetic parameter estimations were then performed afterward based on the averaged values of each cluster. See, for example, hierarchical clustering of the time activity curves (TACs) using a weighted dissimilarity measure [Guo *et al.* \(2003\)](#), and a comparison of a number of different hierarchical clustering algorithms in this context [Velamuru *et al.* \(2005\)](#).

Recently, simultaneous clustering and parameter estimation methods have been proposed using a spatially regularized K -means algorithm. The algorithm iteratively estimates the kinetic parameters in a least squared sense between each cluster update [Saad *et al.* \(2007\)](#). It was demonstrated that incorporating the physiological model in the clustering procedure performed better than their counterparts in terms of clustering. However, the method offers no guidance on the choice of cluster numbers, or how to select the spatial regularization parameter, both can have great influence on the results. A similar algorithm was proposed [Mohy-ud Din *et al.* \(2014\)](#), where the clustering and parameter estimation were performed simultaneously, although spatial correlation was ignored. They demon-

strated improvements to parameter estimation in myocardial perfusion PET imaging.

We develop a fully Bayesian approach, based on defining a finite mixture of multivariate Gaussian distributions to model each voxelwise TAC. We consider that there are a number of distinct homogeneous groups of voxel kinetics which tend to be spatially contiguous. The optimal number of mixture components (or groups) is estimated via information theoretic criteria. This provides a flexible specification of the error distribution for the TAC. Additionally, we model the spatial dependence between the TACs via the Markov random field (MRF), which allows us to borrow information across nearby voxels. Our model simultaneously handles both spatial and temporal information, making full use of the data available, and this is done with the estimation of the kinetic parameters in a single step.

We apply our approach to simulated one-compartment PET perfusion data and compare the performance of our approach with both the standard voxelwise curve-fitting approach and the spatial temporal approach [Saad *et al.* \(2007\)](#), using the true kinetic parameters as the gold standard. We also apply our method to an in vivo pig study data.

2 Materials and Methods

2.1 Simulated Dynamic Cardiac Perfusion PET Data

All the simulation studies were performed using an NCAT torso phantom [Segars \(2000\)](#) which consists of heart, lungs, liver, and soft-tissue compartments. The left ventricle (LV) myocardium was segmented into 17 standard segments. [Cerqueira *et al.* \(2002\)](#) The simulation was based on ^{18}F -flurpiridaz, which is a new myocardial perfusion tracer that exhibits rapid uptake and longer washout in cardiomyocytes. Based on the one-tissue compartmental model, the TAC of the tissue concentration, $C_t(t)$, was simulated using

$$C_t(t) = K_1[C_p(t) \otimes \exp(-k_2t)], \quad (1)$$

where $C_p(t)$ is the blood input function, K_1 and k_2 are kinetic rate constants for the segment, and \otimes denotes convolution operation. The input

function used in the simulation was based on a previously published ^{18}F -flurpiridaz study [Alpert, Dean, and El Fakhri \(2012\)](#). During the study, the LV input function was extracted with generalized factor analysis on dynamic series [El Fakhri, Sitek, Guérin, Kijewski, Di Carli and Moore \(2005\)](#); [El Fakhri, Sitek, Zimmerman and Ouyang \(2006\)](#). This LV input function was treated as the plasma input function.

The kinetic parameters, i.e., $k = (K_1, k_2)$, assigned to 17 segments were based on the realistic values obtained from PET perfusion studies on normal patients. [Alpert, Dean, and El Fakhri \(2012\)](#) In order to mimic a myocardial defect, the segment located in the anterior wall was assigned with values by lowering K_1 and k_2 by 50% and 20%, respectively, of their original values. We added the 18th segment to include other voxels not part of the left ventricle myocardium. Table 1 shows the kinetic parameters assigned to all the 18 segments in the myocardium. The blood input function $C_p(t)$ and TACs for one normal (basal inferoseptal) and one defect (apex) segments are shown in Figure 1.

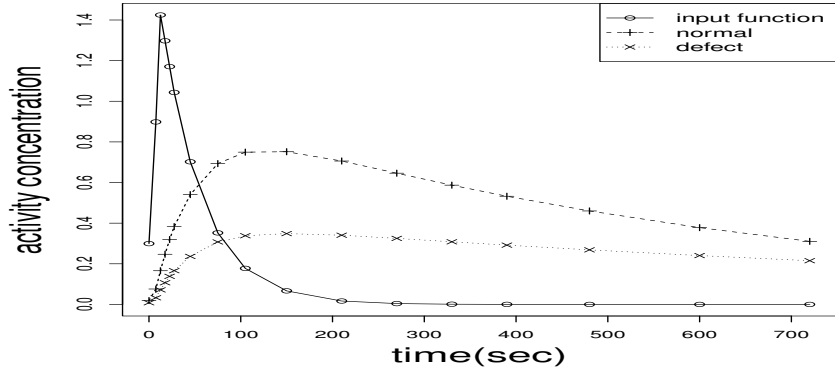


Figure 1: The input function and two TACs (one normal and one defect segment).

A system matrix corresponding to Philips Gemini PET-CT camera, which includes position dependent point spread function modelling, a forward-projection operator implemented using Siddon's method, line of response (LOR) normalization factors, and attenuation correction factors, was used to create noise-free sinograms from TACs. [Petibon et al. \(2013\)](#) The simulated sinogram data is equivalent to a 13-min dynamic PET scan with the framing scheme of $6 \times 5\text{s}$, $3 \times 30\text{s}$, $5 \times 60\text{s}$, and $3 \times 120\text{s}$ frames. Twenty five dynamic PET noise realizations were generated. Both random and

segment	K_1	k_2	segment	K_1	k_2
Basal anterior	0.3665	0.0627	Midinferior	0.7162	0.0799
Basal anteroseptal	0.6730	0.0740	Midinferolateral	0.8013	0.0997
Basal inferospetal	0.7656	0.0983	Midanterolateral	0.7720	0.0861
Basal inferior	0.7487	0.0635	Apical anterior	0.3653	0.0673
Basal inferolateral	0.9655	0.1032	Apical septal	0.8000	0.0861
Basal anterolateral	0.8021	0.0667	Apical inferior	0.7544	0.0717
Midanterior	0.3438	0.0541	Apical lateral	0.6816	0.1044
Midanteroseptal	0.7799	0.0877	Apex	0.3290	0.0554
Midinferoseptal	0.9016	0.0730	Others	0.7630	0.0820

Table 1: Segment names and their assigned K_1 values in mL/min/cc, k_2 values in 1/min (i.e.,the ground truth).

scatter events were not included in this study. The total number of events simulated in all the time frames is 50 M. The decay of the tracer was not simulated. Poisson noise was then added to each pixel in the sinogram based on the mean counts for the pixel. For each noise realization, the image reconstruction at each time frame was performed using standard ordered subset expectation maximization [Hudson and Larkin \(1994\)](#)(OSEM) with 16 subsets and 8 iterations. No postreconstruction smoothing was applied. The physical dimension in the image reconstruction was 57.6cm \times 57.6cm \times 16.2cm, matrix dimension was 128 \times 128 \times 36, where the voxel size was 0.45cm \times 0.45cm \times 0.45cm.

2.2 In-Vivo Pig Study Data

A pig with a body weight of 40 kg was scanned on a Siemens Biograph TruePoint PET/CT with the radiotracer ^{18}F -flurpiridaz. First, a planar x-ray topogram was performed to allow delineation of the field of view (FOV) and centering on the heart following CT and PET acquisitions. The cardiac CT was used for structure localization and later for attenuation correction during reconstruction of PET images. Emission PET data were acquired in 3D list mode and started concomitantly to the injection of ^{18}F -flurpiridaz, the injected activity was 11 mCi at the time of injection. List mode data were framed into dynamic series of 12 \times 5, 8 \times 15, 4 \times 30, 5 \times 60s. PET images were reconstructed using filtered back projection with

minimal filtering (voxel size: 2.14x2.14x3 mm³, 55 slices). Attenuation correction was obtained from the CT images. Decay correction was applied and the first 10 min of the data are used for kinetic analysis. The input functions for the left and right ventricle were obtained by averaging the TACs from a manually defined region. A one-compartment model with spill-over correction was used. The described experiment was performed under a protocol approved by the Institutional Animal Care and Use Committee at the Massachusetts General Hospital.

2.3 Kinetic Parameter Estimation Using Curve Fitting

Kinetic analysis is performed by curve-fitting the TAC in each voxel using a nonlinear least-square fitting,

$$\mathbf{k}_i = \operatorname{argmin} \sum_{t=1}^T w^t (y_i^t - x_i^t(\mathbf{k}_i))^2, \quad (2)$$

where y_i^t is the reconstructed activity concentration for voxel i at time frame t divided by frame duration $\Delta\tau_t = \tau_{t,e} - \tau_{t,s}$, $x_i^t(\mathbf{k}_i) = \frac{1}{\Delta\tau_t} \int_{\tau_{t,s}}^{\tau_{t,e}} K_{1,i}[\hat{C}_p(s) \otimes \exp(-k_{2,i}s)] ds$, is the average concentration over time frame t using the current estimates of the kinetic parameters $\mathbf{k}_i = (K_{1,i}, k_{2,i})$ in voxel i , and measured blood input function $\hat{C}_p(t)$, w^t is the weighting factor which herein is chosen to be the squared frame duration divided by the total counts in that frame [Gunn et al. \(1997\)](#). This nonlinear least-square problem can be solved using the Levenberg-Marquardt algorithm. [Wang and Qi \(2009\)](#) We denote this standard curve-fitting (SCF) approach in this paper.

2.4 Spatial K -means(SKMS)

The spatial SKMS method performs spatial K -means clustering and parameter estimation iteratively [Saad et al. \(2007\)](#). The process is as follows. (1) Initialize the cluster means $\mu_g, g = 1, \dots, G$ for a predetermined number of clusters G . (2) For each g , estimate kinetic parameters $\mathbf{k}_g = \operatorname{argmin} \sum_{t=1}^T (\mu_g(t) - C_t(t, \mathbf{k}_g))^2$; subject to positivity constraints on \mathbf{k}_g . (3) For each voxel indexed by $i = 1, \dots, n$, reassign cluster membership by minimizing the objective function $\sum_{i=1}^n (\sum_{g=1}^G \|y_i - C_t(t, \mathbf{k}_g)\|^2) + \beta \sum_{r=1}^R I(y_i, y_r)$. y_i is the TAC at voxel i . β determines the influence of the spatial regularizer. $I(\cdot)$ is the indicator function returning a one if y_i and y_r belong to the

same cluster and zero otherwise, for all y_r in the neighbourhood of y_i . (4)
Based on the new clusters, calculate μ_g as the mean for each cluster. (5)
Repeat above steps until there are no significant changes in $C_t(t, \mathbf{k}_g)$.

There are two main issues for SKMS. First, the authors offered no theoretical guarantee of convergence of their proposed algorithm. Second, both the number of clusters and spatial regularization parameter β , need to be determined but it is not clear how this can be done. In our implementation of their method, we chose these parameters by looking at a range of β and G values, and selected the values which minimizes the errors with respect to K_1 parameter estimates, setting β to 0.2 and G to 17. We note, however, this procedure produces the best possible outcome for SKMS but is only possible for simulation data where we know the ground truth. This method was not implemented for the pig study data.

2.5 A Bayesian Spatial Mixture Model(SMM)

2.5.1 Model

Here, we describe our proposed modelling and estimation approach. We denote the reconstructed activity concentration data by $y_i = (y_i^1, \dots, y_i^T) \in \mathbb{R}^T$, for voxel i . Each data point y_i^t corresponds to the reconstructed activity concentration at time t . We assume that the data y_i can be grouped into G spatially homogeneous groups, where within each group, all voxels share the same kinetic rate parameters (or TACs) and their variations are only due to noise. The number of groups, G , is treated as unknown and is chosen by the information theoretic model selection criterion, Bayesian information criterion (BIC).

We use a mixture of multivariate Gaussian distribution with G components to model the noisy data. Given the ROI used for the analysis may include some voxels outside the myocardium, as well as some noisy voxels with very little activity uptake inside the myocardium, we allow one component to cluster these types of voxels. We call this the noise component. The Potts model [Wu \(1982\)](#) is used to account for spatial correlation between the TACs. This is achieved by introducing a set of auxiliary random variables $\mathbf{z} = (z_1, \dots, z_n)$, where z_i takes one of the values $1, \dots, G$, and represents the group/cluster membership for each voxel. Mathematically, each noisy TAC is given by the mixture of T -dimensional Gaussian,

$$f(y_i|\boldsymbol{\mu}, \boldsymbol{\Sigma}, \beta) = \sum_{g=1}^G f(z_i = g|\beta)MVN(y_i|z_i = g, \boldsymbol{\mu}_g, \boldsymbol{\Sigma}),$$

where $f(z_i = g|\beta)$ is the marginal density of the Potts model, $MVN(y_i|z_i = g, \boldsymbol{\mu}_g, \boldsymbol{\Sigma})$ is the density of the multivariate Gaussian, and β is the parameter that reflects the spatial strength between voxels. A value of 0 indicates independence between voxels, while larger values of β will tend to cluster all voxels into one cluster. The mean vector of the g th multivariate Gaussian component is denoted by $\boldsymbol{\mu}_g$, and $\boldsymbol{\Sigma} = \text{diag}(\sigma^{2,1}, \dots, \sigma^{2,T})$ is the covariance matrix, assumed to be the same for all mixture components. One may relax this assumption to allow more general covariance structure; however, in our simulations studies, the same covariance structure worked well. Here, $\sigma^{2,t}, t = 1, \dots, T$ denotes the variance at time t , and the data are assumed to be temporally independent as data were based on the reconstructed image at each time frame. The mixture model representation allows the error distribution to be more flexible. We refer to our model as the SMM.

We set the mean vector for the noise component g^* as

$$\boldsymbol{\mu}_{g^*} = (\mu_{g^*}^1, \dots, \mu_{g^*}^T),$$

where the $\mu_{g^*}^t, t = 1, \dots, T$ are unknown parameters. This component is dominated by noise, taking small values compared with other voxels with larger TAC measurements. For the remaining components $g = 1, \dots, G-1$, we model the mean vector as a function of the solution to the ordinary differential equation (ODE) describing the one-compartment model [Morris et al. \(2004\)](#), although extensions to more compartments are straightforward. Hence, for $t = 1, \dots, T$, we set

$$\mu_g^t = \frac{1}{\Delta\tau_t} \int_{\tau_{t,s}}^{\tau_{t,e}} K_1^g \left[\hat{C}_p(s) \otimes \exp(-k_2^g s) \right] ds, \quad (3)$$

where \hat{C}_p is a measured blood input function and $\Delta\tau_t = \tau_{t,e} - \tau_{t,s}$ is the duration of the t th time frame. The parameters K_1^g and k_2^g are the kinetic rate parameters specific for group g .

For the pig study data analyses, we modified Equation 3 to account for

spill-over effects,

$$\mu_g^t = f_{LV}^g \hat{C}_{LV}(t) + f_{RV}^g \hat{C}_{RV}(t) + (1 - f_{LV}^g - f_{RV}^g) \frac{1}{\Delta\tau_t} \int_{\tau_{t,s}}^{\tau_{t,e}} K_1^g \left[\hat{C}_p(s) \otimes \exp(-k_2^g s) \right] ds, \quad (4)$$

where f_{LV}^g and f_{RV}^g denote the component specific spill-over fractions for the left and right ventricle respectively. \hat{C}_{LV} and \hat{C}_{RV} were obtained by manually averaging the TACs from the appropriate ROIs. \hat{C}_p was taken as \hat{C}_{LV} multiplied by the plasma fraction, where the plasma concentration ratio was estimated based on blood samples drawn from previous studies.

2.5.2 Prior Specifications

For Bayesian inference, we need to specify prior distributions for the unknown parameters $K_1^g, k_2^g, \mu_{g^*}^1, \dots, \mu_{g^*}^T, \sigma^{2,1}, \dots, \sigma^{2,T}, \beta, g = 1, \dots, G-1$. We assume independent and uninformative priors for all the parameters, so that the priors are broadly noninformative.

For the kinetic rate parameters, we use the uniform distribution for all g , $K_{1g} \sim \mathcal{U}(a_{K_1}, b_{K_1})$ and $k_{2g} \sim \mathcal{U}(a_{k_2}, b_{k_2})$, where \mathcal{U} denotes uniform distribution. We have used $(a_{K_1}, b_{K_1}) = (0.3, \infty)$ and $(a_{k_2}, b_{k_2}) = (0, \infty)$ in our simulation studies. In real applications, one can sometimes get very abnormal rate constants, and a lower value of a_{K_1} , such as 0.1 used for our pig study data, might be appropriate. Setting a_{K_1} much lower than the plausible ranges for K_1 will result in additional clusters of the noise voxels being estimated with the kinetic model, and will unnecessarily add to computational cost. For the mean vector of the noise component $\mu_{g^*}^t \sim \mathcal{U}(0, \infty)$, $t = 1, \dots, T$. Setting the prior for K_1 sufficiently away from zero allows us to distinguish between the noise component and the non-noise components. We set prior $\beta \sim \mathcal{U}(0, b_\beta)$, where we take b_β to be 1, so as to include most of the plausible values of β . Finally, for the variance parameters $\sigma^{2,t}, t = 1, \dots, T$, we follow the standard approach and use the usual vague conjugate prior with inverse Gamma distribution $\sigma^{2,t} \sim IG(a, b)$, where $a = 0.001, b = 0.001$ for an uninformative prior on $\sigma^{2,t}$. For the pig study data, we define independent priors for the additional parameters $f_{LV}^g \sim U(0, 1)$ and $f_{RV}^g \sim U(0, 1), g = 1, \dots, G$, and set $a_{K_1} = 0.1$ and $b_{K_1} = 1$.

2.5.3 Markov chain Monte Carlo(MCMC)

Bayesian inference proceeds via the posterior distribution, obtained by the simple product of the likelihood and the priors in Section 2.5.2. The likelihood function is given by

$$f(\mathbf{y}, \mathbf{z} | \boldsymbol{\mu}, \boldsymbol{\Sigma}, \beta) = f(\mathbf{z} | \beta) \prod_{i=1}^n f(y_i | z_i, \boldsymbol{\mu}_{z_i}, \boldsymbol{\Sigma}). \quad (5)$$

The posterior distribution is given by the Bayes theorem as the product of the likelihood and the priors

$$f(\mathbf{z}, \boldsymbol{\mu}, \boldsymbol{\Sigma}, \beta | \mathbf{y}) \propto \prod_{i=1}^n f(y_i | z_i, \boldsymbol{\mu}_{z_i}, \boldsymbol{\Sigma}) f(\mathbf{z} | \beta) f(\boldsymbol{\mu}, \boldsymbol{\Sigma}, \beta). \quad (6)$$

where the term $f(\boldsymbol{\mu}, \boldsymbol{\Sigma}, \beta)$ denotes the prior distribution.

MCMC algorithms were developed to sample from the posterior distribution, using a combination of random-walk Metropolis-Hastings and Gibbs updates. Details for the implementation of the algorithm for the model in Equation 3 are given in the Appendix, the model of Equation 4 is a straight forward extension. Note that occasionally identifiability issues arise in the MCMC estimation of mixtures. Parameters from different components can switch labelling as a result of the invariance of the posterior distribution with respect to labelling. This is not an issue when only the MAP estimates are required. The simplest way to handle this is by imposing certain ordering constraints on parameters [Fernández and Green \(2002\)](#), or via postprocessing of the MCMC output [Zhu and Fan \(2015\)](#). In this article, the large number of mixture components was adequately handled using an efficient postprocessing algorithm for MCMC output [Cron and West \(2011\)](#).

2.5.4 Determination of the Number of Components G

One of the uncertainties of the above model is the selection of the value of G , which plays a crucial role in the resulting parameter estimation. For model-based inference, in which a likelihood is readily available, a number of model selection criteria are available, including Bayesian information criterion (BIC), integrated completed likelihood (ICL), deviance information criterion (DIC) and Akaike information criterion (AIC). The BIC is

often considered to be more parsimonious and is the frequently adopted measure of goodness of fit of the model. [Steele and Raftery \(2009\)](#) Our approach uses BIC as the criterion to determine the optimal value of G .

The BIC [Schwarz *et al.* \(1978\)](#) is given as

$$BIC = -2 \log f(\mathbf{y}|G, \hat{\mathbf{z}}_{MAP}, \hat{\theta}_{MAP}) + DF \times (\ln(n) - \ln(2\pi)), \quad (7)$$

where $f(\mathbf{y}|G, \hat{\mathbf{z}}_{MAP}, \hat{\theta}_{MAP})$ is the likelihood function corresponding to the model with G components, evaluated at the MAP estimator of \mathbf{z} and θ , the vector of all remaining unknown parameters. DF is the number of parameters to be estimated, which includes all the unknown kinetic parameters for each cluster, the variance parameters, and any hyperpriors which are estimated. n is the number of observations or voxels. BIC penalizes models with too many parameters against the maximized log-likelihood (or fit to the data). Optimal choice of G corresponds to the model with the smallest BIC value.

2.5.5 Implementation

We tuned the Gaussian random-walk proposal distributions to obtain an optimal overall acceptance probability of around 20%-40%. For the simulation data sets, we used $K_1^{g'} \sim N(K_1^g, 0.006^2)$, $k_2^{g'} \sim N(k_2^g, 0.001^2)$, $\mu_{g^*}^{t'} \sim N(\mu_{g^*}^t, 0.00013^2)$ and $\beta' \sim N(\beta, 0.002^2)$. For the pig data, we used $K_1^{g'} \sim N(K_1^g, 0.005^2)$, $k_2^{g'} \sim N(k_2^g, 0.003^2)$, $\mu_{g^*}^{t'} \sim N(\mu_{g^*}^t, 0.001^2)$, $f_{LV}^{g'} \sim N(f_{LV}^g, 0.01^2)$, $f_{RV}^{g'} \sim N(f_{RV}^g, 0.01^2)$ and $\beta' \sim N(\beta, 0.004^2)$.

For a full Bayesian analysis of a single simulated data set, we ran MCMC for 10000 iterations with the first 4000 iterations discarded as burn-in, and we keep every tenth sample due to high autocorrelation in the MCMC sample. Note that for MAP estimates, taken as the set of parameter values which gave the highest posterior probability during the MCMC run, we used only 6000 iterations, as MCMC chains can be expected reach modal regions of the posteriors quite quickly. For the real data set, 8000 iterations of MCMC were obtained with the first 6000 discarded as burn-in.

We first determine the number of components G , by running MCMC for $G = 2, \dots, 26$ and computing the model selection criteria based on BIC (see Section 2.5.4). Then for a fixed G , we run posterior inference for a given dataset. For the evaluation of the proposed algorithm, we used 25 replicate simulations. For each replication at the chosen value of G , we

obtain MAP estimators for comparison with SCF and SKMS. The performance of MAP is known to be worse than the posterior mean estimate, but it is sufficient to provide a good guide on the quality of the inference. The results are presented in Section 3.

2.6 Performance Evaluation

For a given noise realization, n , we compute kinetic parameter bias of voxel i using

$$b_i^n = (\mathbf{k}_i^n - \mathbf{k}_i^{Tr}) / (\mathbf{k}_i^{Tr}), \quad (8)$$

where b_i^n is the bias of estimated kinetic parameter using the true kinetic parameter \mathbf{k}_i^{Tr} as gold standard. Based on 25 noise realizations, we compute the mean bias \bar{b}_i , the mean squared bias \bar{b}_i^2 , and standard deviation s_i bias for voxel i using

$$\bar{b}_i = \frac{\sum_{n=1}^N b_i^n}{N}, \quad \bar{b}_i^2 = \frac{\sum_{n=1}^N (b_i^n)^2}{N}, \quad s_i = \sqrt{\frac{\sum_{n=1}^N (b_i^n - \bar{b}_i)^2}{N - 1}}, \quad (9)$$

where N is the total number of noise realizations. We perform the calculations described above for SCF, SMM and SKMS methods and make a comparison between methods.

3 Results

3.1 Model Selection

Figure 2 shows the BIC values (left panel) and the corresponding log likelihood (right panel) for competing models for a single noise realization. Horizontal lines in both subfigures denote the minimum and maximum values for BIC and the log likelihood respectively. The log likelihood values are expected to keep increasing with G , while the BIC penalizes the use of additional parameters in models with larger G . Both the BIC and log likelihood changed dramatically from $G = 2$ to about $G = 10$, preferring models with larger G values, and this stabilized after around $G = 17$. Part of the changes seen here can be attributed to Monte Carlo errors. Thus, a parsimonious choice for G would be $G = 17$, representing the model with 16 TAC components and one noise component. Subsequent results

for simulated data in this paper were generated by the model with $G = 17$. The same value of G was also found for the pig study data.

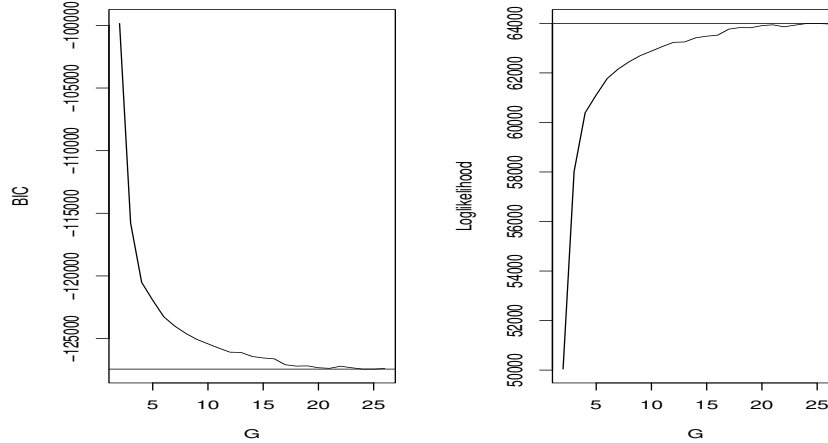


Figure 2: BIC values (left panel) and log likelihood (right panel) for $G = 2, 3, \dots, 26$ in the spatial mixture model. The horizontal lines indicate the minimum and the maximum of BIC and log likelihood respectively.

3.2 Parameter Estimation and Comparison to Existing Methods

For the simulation data, Figures 3 and 4 show the corresponding marginal posterior distributions of K_1 and k_2 respectively, with vertical lines indicating the posterior mean, and the uncertainty of the estimates indicated by the spread of the distributions.

To assess the robustness of our estimation procedure and its performance against existing methods, we repeated our estimation procedure for 25 replicate data sets, obtained from the same simulation setup. We implemented the three competing methods SMM, SCF and SKMS. There was a single extremely large value of k_2 estimate from SKMS, which we omit from the results shown. Figure 5 shows the distribution of the mean squared biases of K_1 and k_2 in the abnormal, normal and noise regions, and the overall standard deviation of the biases. The computations were calculated according to Equation 9, with the exception that in the noise region, the bias was computed by setting the denominator of Equation 8, k_i^{Tr} , to 1, since we cannot divide by zero.

Results for the abnormal ROI are shown in the first row of Figure 5. For K_1 , the mean squared biases for SMM ranged from 0.006 to 0.12, with a median of 0.04. For SCF, the range was from 0.013 to 0.175, with a median of 0.06. For SKMS, the range was between 0.02 and 0.39, and the median was 0.06. For the k_2 estimation, the biases ranged from 0.06 to 1.12 for SMM, the median was 0.25. For SCF, the range was between 0.13 and 1.47, and the median was 0.4. For SKMS, the biases ranged from 0.14 to 0.7, and the median was 0.31.

The normal ROI is shown in the second row of Figure 5. For K_1 , the mean squared biases for SMM ranged from 0.006 to 0.29, with a median of 0.03. For SCF, the range was 0.005 to 0.27, with a median of 0.03. For SKMS, the range was between 0.007 and 0.33, and the median was 0.04. For the k_2 estimation, the biases ranged from 0.01 to 0.37 for SMM, with a median of 0.09. For SCF, the range was between 0.01 to 0.55, and a median of 0.1. For SKMS, the biases ranged from 0.02 to 0.32, and the median was 0.09.

The noise region is shown in the third row of Figure 5. For K_1 , the mean squared biases for SMM ranged from 0.004 to 0.165, with a median of 0.007. For SCF, the range was 0.0001 to 3.32, with a median of 0.02. For SKMS, the range was between 0.0005 and 0.22, and a median of 0.05. For the k_2 estimation, the biases were approximately 0 for SMM. For SCF, the biases ranged between 0 to 0.06, and the median was 0.03. For SKMS, the biases ranged from 0 to 13.05, and the median was 2.96.

The last row of Figure 5 shows the standard deviations of the biases for K_1 and k_2 . For K_1 , the standard deviations of biases ranged from 0 to 0.34 for SMM, with a median of 0. For SCF, the range was between 0.008 to 1.70, with a median of 0.13. For SKMS, the range was between 0.073 to 0.63, and the median was 0.16. For the k_2 standard deviations of bias, the range was between 0 and 0.93 for SMM, with a median of 0. For SCF, the range was between 0.002 to 1.19, and a median of 0.01. For SKMS, the range was between 0.02 and 2.89, with a median of 1.20.

Figure 6 compares the bias and standard deviation of bias between SMM, SCF and SKMS for a single slice. The bias is calculated according to the first term in Equation 9, this is the average of the biases over 25 replications. Figure 6a shows the K_1 estimates. The biases ranged from -0.27 to 0.10, -0.28 to 0.09 and -0.33 to 0.08 respectively, for SMM, SCF and SKMS. Similarly, the standard deviations ranged from 0 to 0.26, 0 to 0.37 and 0 to 0.35 respectively. For the k_2 estimates in Figure 6b, the biases ranged

from -0.22 to 0.2, -1 to 1.06 and -0.46 to 0.28 respectively. The standard deviations ranged from 0 to 0.59, 0 to 0.86 and 0 to 2.89 respectively.

Figure 7 compares a single slice of the kinetic parametric images between SMM and SCF for the pig study. K_1 parameters were constrained to be between 0 and 1 in both SMM and SCF estimation, as unconstrained estimation lead to many physiologically implausible large values of K_1 .

4 Discussions

This paper proposes a novel method, SMM, that clusters voxelwise TACs and estimates kinetic parameters simultaneously. Our modelling approach shares similarities to the recently proposed work [Lin *et al.* \(2014\)](#), where the mixture model was fitted to each voxel (while still borrowing information across nearby voxels) to overcome the issue of non-Gaussian error distributions. We allow several similar voxels to share the same parameter values, since separate mixture models fitted to each voxel introduces too many parameters, and will lead to more estimation uncertainty. Our approach naturally allows us to constrain parameter estimates without the need to specify regularization parameters as in the usual Bayesian maximum a posterior (MAP) approaches. Finally, we allow the data to determine the most appropriate number of mixtures to fit to the data.

Our model-based approach offers several advantages, compared to other existing statistical approaches described above. We require minimal user input in the algorithm, preferring to allow the data to dictate the optimal choices. One benefit of our modelling approach is in the determination of the optimal number of mixture components. We also automatically compute the value of the smoothing parameter used in the MRF model. This unknown parameter is difficult to estimate, and in many applications of spatial modelling, the estimation of this parameter has not been carefully considered. The choice of both these parameters can have a big impact on results, since suboptimal choices will either result in higher bias or higher variance for the resulting parameter estimates. Finally, the Bayesian statistical framework allows us to quantify uncertainty probabilistically, since uncertainty in the model and parameters is a natural consequence of our modelling framework. An efficient MCMC algorithm allows us to provide parameter estimates, as well as uncertainty quantification simultaneously.

In Figure 2, the BIC values start to reach a minimum at around $G = 16$

or 17. We chose to work with 17, but higher values of 18 or 19 will work equally well. These numbers are similar to the number of true segments simulated; however, we expect that this number can be different depending on the nature of the noise. Figures 3 and 4 indicate the component mean estimates for K_1 and k_2 . It is difficult to make direct correspondences between the clusters we obtained with the true segments. The first four components correspond mostly to noise, the next four components correspond mostly to abnormal voxels and the rest belong to normal voxels. The discrepancy between the estimated values of K_1 and the truth is most obvious in the abnormal region, this is possibly a combination of partial volume effect, as well as misclassification of the normal voxels. Given that SMM outperforms the other two methods in the abnormal region, we believe similar issues with the data are affecting the other two methods also. Despite the fact that it is difficult to make sense of individual clusters, aggregating the clusters can provide us with information about the larger ROIs. For instance, if we are interested in identifying the three regions of noise, abnormal and normal, we can aggregate the clusters according to $K_1 < 0.3$, $0.3 \leq K_1 < 0.6$ and $K_1 \geq 0.6$ respectively. A similar procedure can be used to classify the regions using the results from SCF and SKMS. In terms of misclassification rates, based on a single simulation data set, SMM classified 96.34% of noise voxels correctly, compared to 94.43% and 87.60% for SCF and SKMS. The misclassified voxels for SMM were all assigned to the abnormal voxels, this corresponds to the first four clusters in Figure 3. For the other two methods, they were spread between abnormal and normal voxels. For the abnormal region, SMM had a 100% correct classification, while this was only 62.68% for SCF and 52.82% for SKMS. All of the misclassifications in SCF and SKMS were allocated to noise. Finally, for the normal region, SMM, SCF and SKMS had 69.57%, 73.49% and 58.99% respectively for correct classifications, most of the misclassifications were found to be allocated to the abnormal region.

In terms of k_2 estimation, SMM is clearly better than the other two methods. This can be seen clearly in Figures 5 and 6. SKMS performed the worst, particularly in the abnormal and noise regions, their parameter estimation can be prone to very large biases. In the noise region, in particular, the median mean squared bias was around 2.96, while the other two methods were close to 0. Putting constraints on these parameters may prove useful.

For K_1 estimates, SKMS was marginally worse than the other two meth-

ods in terms of mean squared bias. In the abnormal region, SMM shows noticeably superior performance, where it can be seen in Figure 5, top row, the entire distribution of SMM is closer toward 0 than the other two methods. The difference in the normal region is less obvious. The third row in Figure 5 shows the biases in the noise region; here, since SMM set K_1 in this region to 0, the graph can be interpreted by looking separately at the values of mean squared bias below $(0.3)^2 = 0.09$ and above. On average, voxels with bias greater than this value are essentially misclassified, i.e., they should be singled out as noise, but instead have significant values for the kinetic parameters. For SMM, there was an average misclassification rate of 3.66%, for SCF it is 5.71% and 11.65% for SKMS. SCF has the largest mean squared biases here, going up to 3.32, while the other two methods remain around 0.2.

In terms of the standard deviations of the bias, SMM performed the best, while SCF was the worst. The plot in the last row of Figure 5 shows that for K_1 , the range for SCF goes up to 1.7, while for SMM and SKMS, this was only 0.34 and 0.63 respectively. In fact, 15% of the voxels estimated by SCF was greater than 0.34 (the largest value obtained by SMM), and 0.8% from SKMS.

The proposed method is clearly superior in terms of robustness, indicated by the substantially smaller standard deviation estimates, as can be seen in both Figure 5 and Figure 6. It also performed at least as good as, and sometimes better than the other two methods in terms of mean squared bias. In the single slice plot in Figure 6, where the mean of the raw biases was plotted, it is difficult to distinguish between the three methods. This is due to the fact that when raw biases are averaged, they will go toward zero as the effects of the large positive and negative biases cancel out. This will be true for all unbiased estimators regardless of how sensitive the estimations are to noise. In this sense, it is more useful to look at the mean squared or absolute biases.

In terms of the estimation of the pig study data, it was not possible to compare the bias and standard deviations of the biases because the ground truth was not known. However, the parametric images shown in Figure 7 suggest that much smoother K_1 and k_2 images were produced by SMM compared to SCF. The white color in the K_1 images indicates a value close to 1, which is the upper bound of the artificial constraint we used. It is clear from the figure that many values produced by the SCF method were simply truncated at this value. SMM estimation produced significantly less

values close to the upper bound. The upper bound of 1 for K_1 is essentially arbitrary. For SMM estimation, if we remove this bound, we obtain two groups of voxels with physiologically implausibly high K_1 values whilst the rest of the voxel estimates remains unchanged, well below 1. However, in terms of the SCF estimation, raising the bounds to higher than 1 produced many more voxels between 1 and 2. However, since this was a resting pig, where the mean blood flow at rest is around 0.65 ml/min/cc, we do not expect flow to be above 1 at rest, so the SCF results with higher bounds would be difficult to interpret, since the higher values could also be due to spill-over from blood-pools, or voxels actually containing blood or noise.

In terms of computation, it took about 4 hours to complete all 6000 iterations for each noise realization of simulated data, using Matlab R2014b, running on a single node of the Linux computational cluster Katana at UNSW, Australia. This is equivalent to running on an average PC. The total number of voxels was 5746. We found that all the parameters converged quite quickly. For SCF and SKMS, the computational time was around 1 minute. For the pig study data involving 16821 voxels, and a longer time series involving 29 time points, the computational times were 23.5 hours and 6 hours for SMM and SCF respectively. We note that although SMM is computationally more expensive, it provides additional uncertainty estimation, which the other two faster methods do not. Parallel computation or other computational methods, such as variational Bayes [Attias \(2000\)](#), can be adopted to further speed up this process.

In the future, there are three directions to be considered to further develop our approach. First, we can relax the within cluster homogeneity assumption. This is easily achievable by relaxing the mean of the normal mixture to allow them to vary for each voxel observation. However, this substantially increases the number of parameters that needs to be estimated and presents a computational challenge. Second, we can consider the use of sinogram data rather than reconstructed data to estimate kinetic parameters, and this can reduce the additional noise introduced through the reconstruction step; however, this approach can be computationally challenging for full Bayesian analyses. Third, given its flexibility, SMM can be easily extended to more advanced kinetic models, such as the two-compartment tissue model without too much modification. Although we assess performance using simulations of cardiac perfusion PET imaging and demonstrate in vivo data for this application, our approach is not lim-

ited to this specific context and may also benefit other dynamic PET procedures as well as dynamic SPECT, dynamic contrast enhanced CT (DCE-CT), and dynamic contrast enhanced MR (DCE-MR).

5 Conclusion

This paper proposed a novel spatiotemporal approach, SMM, to infer parametric PET images. By borrowing information from nearby voxels, SMM can be used to simultaneously estimate kinetic parameters and classify voxels with similar kinetic parameters into spatially homogeneous groups. We adopted the MRF to incorporate the spatial dependence of voxels. We developed an efficient MCMC algorithm for the computation, which estimates all unknown parameters, including the notoriously difficult spatial smoothness parameter β in the Potts model. The method provides parameter uncertainty estimation, as well as a principled way to determine the optimal number of voxel groups. We used simulated cardiac perfusion PET data to evaluate the performance of SMM and compared them with SCF and SKMS. SMM was substantially less sensitive to noise than the other methods, it also yielded an overall smaller bias than SCF and SKMS. In the pig study data, SMM was shown to produce smoother parametric images compared to the standard curve fitting. Although simulation and experimental data were based on cardiac PET studies of a one-compartment model, the approach may benefit other dynamic PET procedures, as well as more complex compartmental models.

Acknowledgements

This research was supported in part by UNSW 2014 Science Silver Star grant and NIH grants R01-HL118261, R01-HL110241, and NIH T32EB013180.

Appendix

Markov chain Monte Carlo

We use MCMC for sampling from the joint posterior distribution of \mathbf{z} and all other parameters, given by Equation 6. The prior distribution $f(\boldsymbol{\mu}, \boldsymbol{\Sigma}, \beta)$ is taken as product of the individual prior components $f(K_1^1), \dots, f(K_1^{G-1}), f(k_2^1), \dots, f(\sigma^{2,1}), \dots, f(\sigma^{2,T}), f(\beta)$, as defined in Section 2.5.2.

The first term on the right side of Equation 6 is given by

$$\begin{aligned} f(y_i | z_i = g, \boldsymbol{\mu}_g, \boldsymbol{\Sigma}) \\ = (2\pi)^{-T/2} |\boldsymbol{\Sigma}|^{-1/2} \exp\left(-\frac{1}{2}(y_i - \boldsymbol{\mu}_g)' \boldsymbol{\Sigma}^{-1} (y_i - \boldsymbol{\mu}_g)\right), \end{aligned}$$

and the second term on the right side of the equation is given by

$$f(\mathbf{z} | \beta) = \frac{1}{C(\beta)} \exp\left\{\beta \sum_{i \sim j} I(z_i = z_j)\right\}.$$

This is the Potts model, where $\mathbf{z} = (z_1, \dots, z_n)$, $I(\cdot)$ denotes indicator function taking value 1 if $z_j^{(l-1)} = g$ and 0 otherwise, and $i \sim j$ denotes the voxels j in the neighbourhood of voxel i . The partition function $C(\beta)$ is estimated offline using thermal dynamic integration. [Green and Richardson \(2002\)](#) We use an 8 nearest neighbour first order structure for the Potts model.

Our computational algorithm for the one-compartmental model in Equation 3 proceeds as follows:

Step 1 Set $l = 1$ and initialise parameters $K_1^{1,(0)}, k_2^{1,(0)}, \dots, K_1^{G-1,(0)}, k_2^{G-1,(0)}, \boldsymbol{\mu}_{g^*}^{(0)}, \sigma^{2,1,(0)}, \dots, \sigma^{2,T,(0)}, \mathbf{z}^{(0)}, \beta^{(0)}$.

Step 2 Update K_1^g , for $g = 1, \dots, G - 1$. Simulate a new value

$$K_1'^g \sim N(K_1^{g,(l-1)}, \delta_{K_1}^2)$$

and compute $\boldsymbol{\mu}'_g$ with $K_1'^g$, according to Equation (3). Set $K_1^{g,(l)}$ to $K_1'^g$ with probability α , where

$$\alpha = \min\{1, \alpha^*\}$$

with

$$\alpha^* = \frac{\prod_{i \in \{i: z_i^{(l-1)} = g\}} f(y_i | z_i^{(l-1)}, \boldsymbol{\mu}'_g, \boldsymbol{\Sigma}^{(l-1)}) f(K_1'^g)}{\prod_{i \in \{i: z_i^{(l-1)} = g\}} f(y_i | z_i^{(l-1)}, \boldsymbol{\mu}_g^{(l-1)}, \boldsymbol{\Sigma}^{(l-1)}) f(K_1^{g, (l-1)})}$$

Otherwise, set $K_1^{g, (l)}$ to $K_1^{g, (l-1)}$.

Step 3 Update k_2^g , For $g = 1, \dots, G - 1$. Analogously to Step 2.

Step 4 Update $\mu_{g^*}^t$, for $t = 1, \dots, T$. Simulate a new value

$$\mu_{g^*}^t \sim N(\mu_{g^*}^{t, (l-1)}, \delta_{\mu_{g^*}}^2).$$

Set $\mu_{g^*}^{t, (l)}$ to $\mu_{g^*}^t$ with probability α , where

$$\alpha = \min\{1, \alpha^*\}$$

with

$$\alpha = \frac{\prod_{i \in \{i: z_i^{(l-1)} = g^*\}} f(y_i | z_i^{(l-1)}, \boldsymbol{\mu}'_{g^*}, \boldsymbol{\Sigma}^{(l-1)}) f(\mu_{g^*}^t)}{\prod_{i \in \{i: z_i^{(l-1)} = g\}} f(y_i | z_i^{(l-1)}, \boldsymbol{\mu}_{g^*}^{(l-1)}, \boldsymbol{\Sigma}^{(l-1)}) f(\mu_{g^*}^{t, (l-1)})}$$

Otherwise, set $\mu_{g^*}^{t, (l)}$ to $\mu_{g^*}^{t, (l-1)}$.

Step 5 Update $\sigma^{2, t}$, for $t = 1, \dots, T$. Simulate from the Inverse Gamma distribution

$$\sigma^{2, t, (l)} \sim IG\left(n/2 + a, \frac{1}{2} \sum_{i=1}^n (y_i^t - \mu_g^{t, (l)})^2 + b\right).$$

Step 6 Update \mathbf{z} . Each $i = 1, \dots, N$, compute

$$w_g = MVN(y_i; f(K_1^g, k_2^g), \boldsymbol{\Sigma}) \exp\{\beta^{(l-1)} \sum_{j, j \in \partial i} I(z_j^{(l-1)} = g)\}, \quad g = 1, \dots, G,$$

and normalise $w'_g = w_g / \sum_{g=1}^G w_g$, where $f(K_1^g, k_2^g)$ denotes Equation 3. ∂i denotes the set of neighbours of vertex i . Set $z_i^{(l)}$ according to the Multinomial distribution

$$z_i^{(l)} \sim MN(w'_1, \dots, w'_G).$$

Step 7 Update β . Simulate a new value

$$\beta' \sim N(\beta^{(l-1)}, \delta_\beta^2)$$

and set $\beta^{(l)}$ to β' with probability α , where

$$\alpha = \min \left\{ 1, \frac{f(\mathbf{z}^{(l)}|\beta')f(\beta')}{f(\mathbf{z}^{(l)}|\beta^{(l-1)})f(\beta^{(l-1)})} \right\}.$$

Otherwise, set $\beta^{(l)}$ to $\beta^{(l-1)}$.

Step 8 set $l = l + 1$, if $l < L$, go to Step 2.

References

- N. Alpert, Y. Dean, and G. El Fakhri, "Single-scan rest/stress imaging ^{18}F -labeled flow tracers," *Medical Physics* **39**, 6609 – 6620 (2012).
- H. Attias, "A variational Bayesian framework for graphical models," *Advances in neural information processing systems* **12**, 209–215 (2000).
- M. D. Cerqueira, N. J. Weissman, V. Dilsizian, A. K. Jacobs, S. Kaul, W. K. Laskey, and et al., "Standardized Myocardial segmentation and nomenclature for tomographic imaging of the heart: A statement for healthcare professionals from the Cardiac Imaging Committee of the Council on Clinical Cardiology of the American Heart Association," *J Nucl Cardiol* **9**, 240–245 (2002).
- A. J. Cron and M. West, "Efficient classification-based relabeling in mixture models," *The American Statistician* **65**, 16–20 (2011).
- G. El Fakhri, A. Sitek, B. Guéin, M.F. Kijewski, M.F. Di Carli, and S. C. Moore, "Quantitative dynamic cardiac ^{82}Rb PET using generalised factor and compartment analyses," *J. Nucl. Med.* **48**, 1264 – 1271 (2005).
- G. El Fakhri, A. Sitek, R.E. Zimmerman, and J. Ouyang, "Generalised five dimensional dynamic and spectral factor analysis," *Med. Phys.* **33**, 1016 – 1024 (2006).
- C. Fernández and P. J. Green, "Modelling spatially correlated data via mixtures: a bayesian approach," *Journal of the royal statistical society: series B (Statistical methodology)* **64**, 805–826 (2002).
- P. J. Green and S. Richardson, "Hidden Markov Models and disease mapping," *Journal of the American statistical association* **97**, 1055–1070 (2002).
- R. N. Gunn, A. A. Lammertsma, S. P. Hume, and V. J. Cunningham, "Parametric imaging of ligand-receptor binding in PET using a simplified reference region model," *Neuroimage* **6**, 279–287 (1997).
- R. N. Gunn, S. R. Gunn, F. E. Turkheimer, J. A. Aston, and V. J. Cunningham, "Positron Emission Tomography compartmental models; a basis

- pursuit strategy for kinetic modelling," *Journal of Cerebral Blood Flow & Metabolism* **22**, 1425–1439 (2002).
- H. Guo, R. Renaut, K. Chen, and E. Reiman, "Clustering huge data sets for parametric PET imaging," *BioSystems* **71**, 81–92 (2003).
- S.-C. Huang and Y. Zhou, "Spatially-coordinated regression for image-wise model fitting to dynamic PET data for generating parametric images," *Nuclear Science, IEEE Transactions on* **45**, 1194–1199 (1998).
- H. M. Hudson and R. S. Larkin, "Accelerated image reconstruction using ordered subsets of projection data," *Medical Imaging, IEEE Transactions on* **13**, 601–609 (1994).
- M. E. Kamasak, C. A. Bouman, E. D. Morris, and K. Sauer, "Direct reconstruction of kinetic parameter images from dynamic pet data," *Medical Imaging, IEEE Transactions on* **24**, 636–650 (2005).
- A. A. Lammertsma and S. P. Hume, "Simplified reference tissue model for PET receptor studies," *Neuroimage* **4**, 153–158 (1996).
- Y. Lin, J. Haldar, Q. Li, P. Conti, and R. Leahy, "Sparsity constrained mixture modelling for the estimation of kinetic parameters in dynamic PET," *IEEE Trans Med Imaging* **33** (2014).
- H. Mohy-ud Din, N. A. Karakatsanis, M. A. Lodge, J. Tang, and A. Rahmim, "Parametric myocardial perfusion pet imaging using physiological clustering," in *SPIE Medical Imaging* (International Society for Optics and Photonics, 2014) pp. 90380P–90380P.
- E. D. Morris, C. J. Endres, K. C. Schmidt, B. T. Christian, R. F. Muzic Jr., and R. E. Fisher, "Emission tomography," (Elsevier, 2004) Chap. Kinetic modelling in positron emission tomography, pp. 499–540.
- J. A. Nye, J. R. Votaw, N. Jarkas, D. Purselle, V. Camp, J. D. Bremner, C. D. Kilts, C. B. Nemeroff, and M. M. Goodman, "Compartmental modelling of 11c-homadam binding to the serotonin transporter in the healthy human brain," *Journal of Nuclear Medicine* **49**, 2018–2025 (2008).
- F. O'Sullivan and A. Saha, "Use of ridge regression for improved estimation of kinetic constants from PET data," *Medical Imaging, IEEE Transactions on* **18**, 115–125 (1999).

- Y. Petibon, J. Ouyang, X. Zhu, C. Huang, T. G. Reese, S. Y. Chun, Q. Li, and G. El Fakhri, "Cardiac motion compensation and resolution modelling in simultaneous PET-MR: a cardiac lesion detection study," *Physics in Medicine and Biology* **58**, 2085–2102 (2013).
- A. Saad, B. Smith, G. Hamarneh, and T. Möller, "Simultaneous segmentation, kinetic parameter estimation, and uncertainty visualization of dynamic PET images," in *Medical Image Computing and Computer-Assisted Intervention—MICCAI 2007* (Springer, 2007) pp. 726–733.
- G. Schwarz *et al.*, "Estimating the dimension of a model," *The Annals of Statistics* **6**, 461–464 (1978).
- W. Segars, *Development of a new dynamic NURBS-based cardiac torso (NCAT) phantom*, Ph.D. thesis, University of North Carolina (2000).
- M. Slifstein, B. Kolachana, E. Simpson, P. Tabares, B. Cheng, M. Duvall, W. G. Frankle, D. Weinberger, M. Laruelle, and A. Abi-Dargham, "COMT genotype predicts cortical-limbic D1 receptor availability measured with ^{11}C ; NNC112 and PET," *Molecular psychiatry* **13**, 821–827 (2008).
- R. J. Steele and A. E. Raftery, "Performance of Bayesian model selection criteria for Gaussian mixture models," *Bayesian Analysis*, 113-130 (2010).
- P. K. Velamuru, R. A. Renaut, H. Guo, and K. Chen, "Robust clustering of positron emission tomography data," in *In Joint Conference of the Classification Society of North America and INterface Foundation of North America* (2005).
- G. Wang and J. Qi, "Generalized algorithms for direct reconstruction of parametric images from dynamic PET data," *IEEE Trans Med Imaging* **28**, 1717–26 (2009).
- F.-Y. Wu, "The Potts model," *Reviews of modern physics* **54**, 235 (1982).
- Y. Zhou, J. A. Aston, and A. M. Johansen, "Bayesian model comparison for compartmental models with applications in positron emission tomography," *Journal of Applied Statistics* **40**, 993–1016 (2013).

W. Zhu and Y. Fan, "Relabelling algorithms for mixture models with applications for large data sets," *Journal of Statistical Computation and Simulation*, 1–20 (2015).

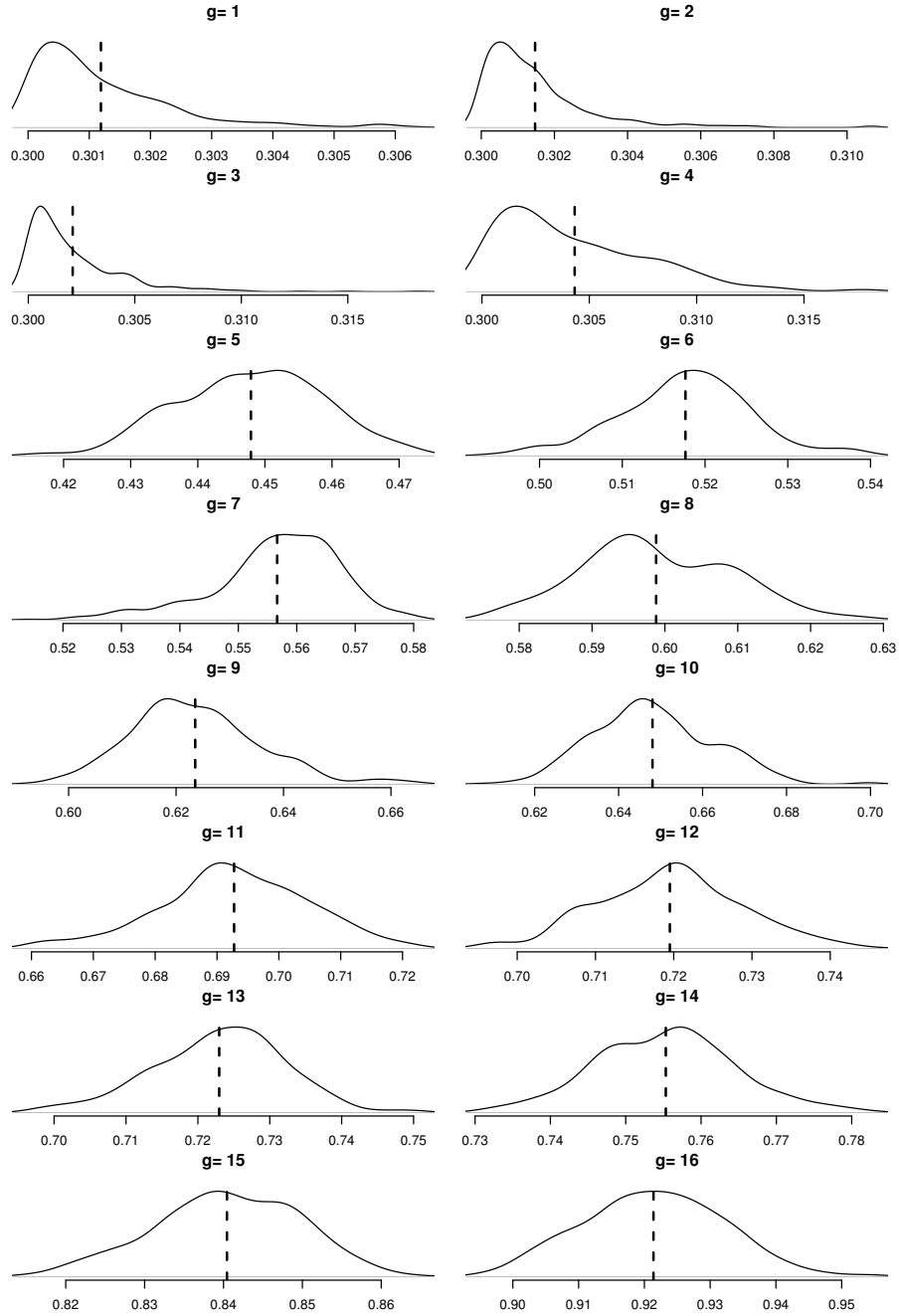


Figure 3: Marginal posterior density of K_1^g for $g = 1, \dots, 16$ clusters. Vertical dashed line denotes corresponding posterior means. Based on a single noise realization of simulation data.

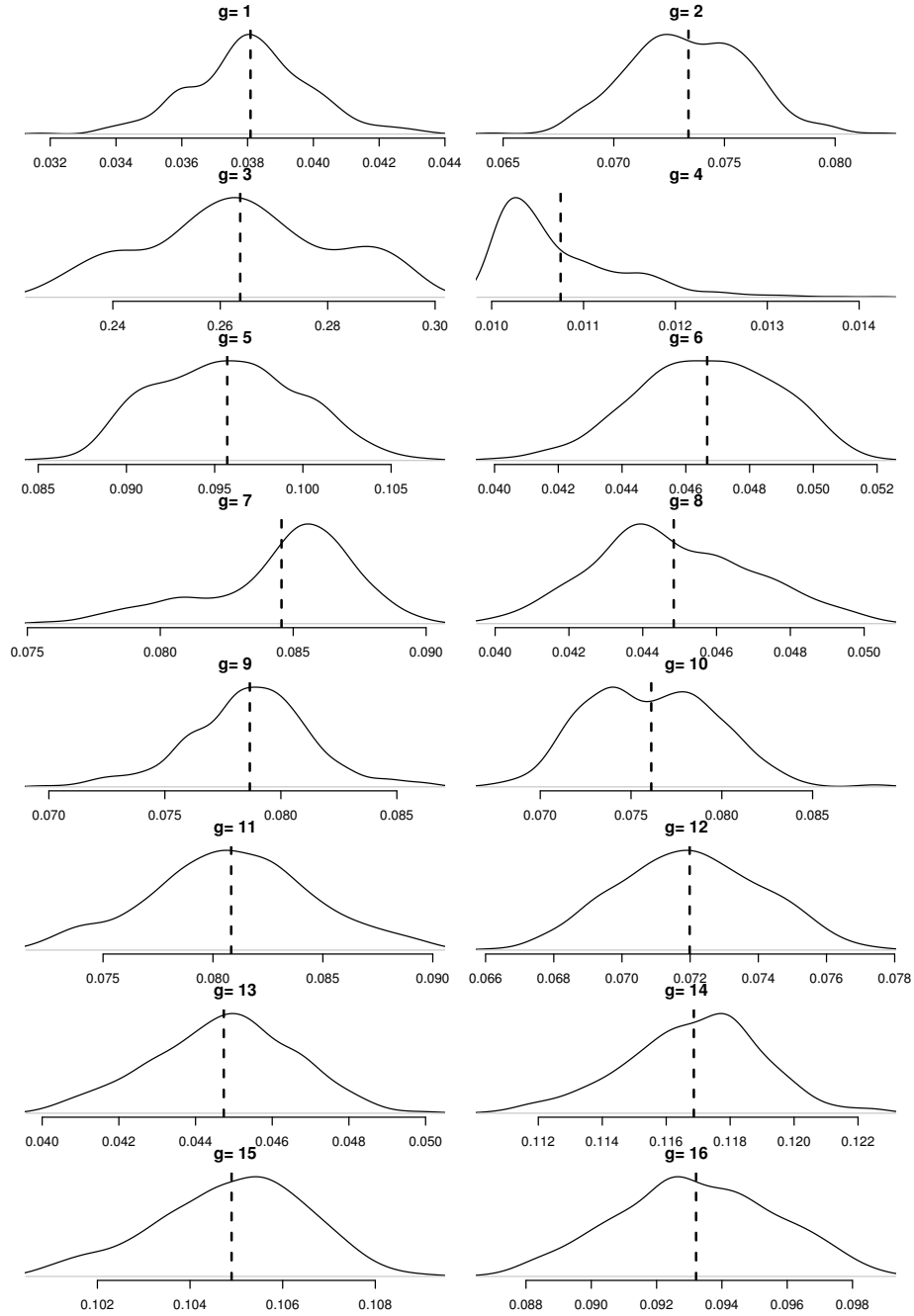


Figure 4: Posterior density of k_2^g for $g = 1, \dots, 16$ clusters. Vertical dashed line denotes corresponding posterior means. Based on a single noise realization of simulation data.

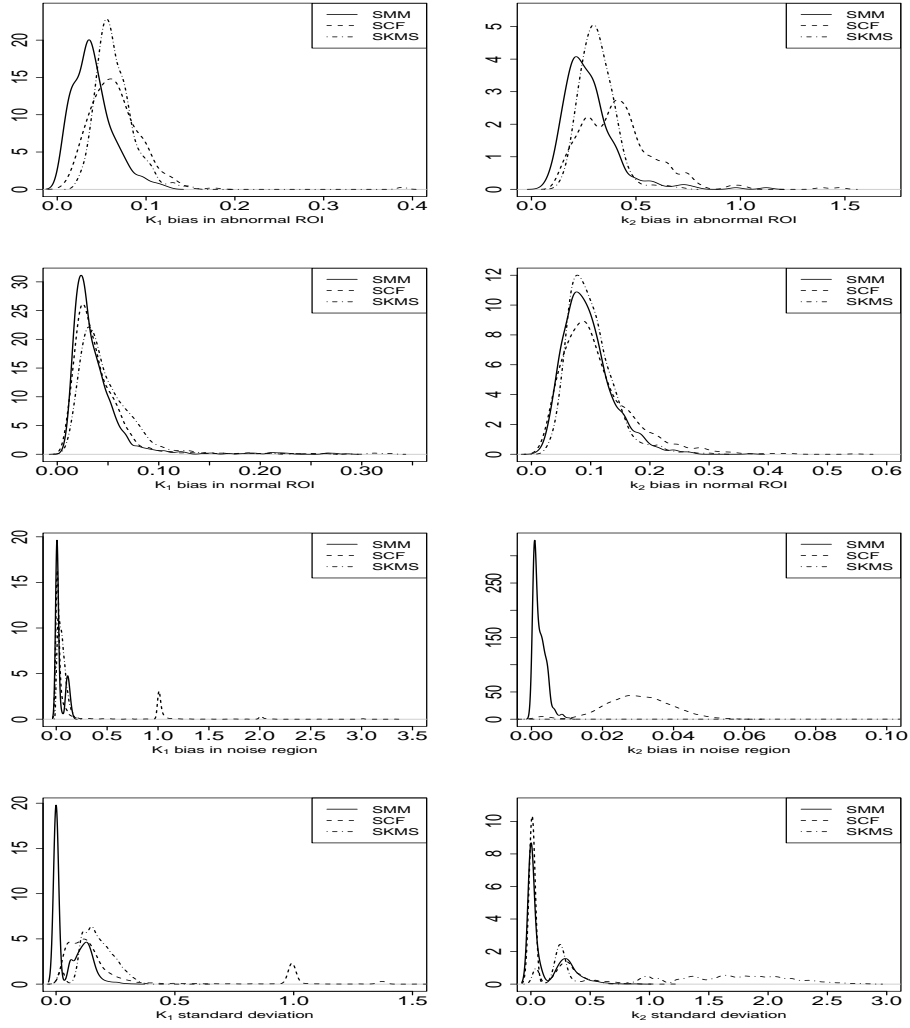


Figure 5: Distributions of the mean squared biases and standard deviation of biases for SMM (solid line); SCF (dashed line) and SKMS (dotted and dashed line). The first three rows show the mean squared biases for K_1 and k_2 in the abnormal, normal, and the noise ROIs respectively. The last row shows the standard deviation of the biases. Mean squared biases and the standard deviation of biases are calculated according to Equations 8 and 9, over 25 replicate simulation data sets.

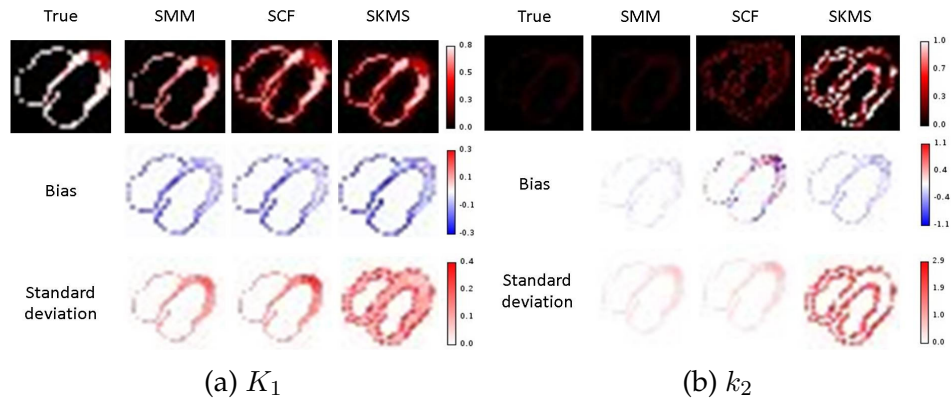


Figure 6: Parameter estimates, bias and standard deviation of bias for a single slice of the image. Comparisons for K_1 (a) and k_2 (b) for 25 replications of simulation data.

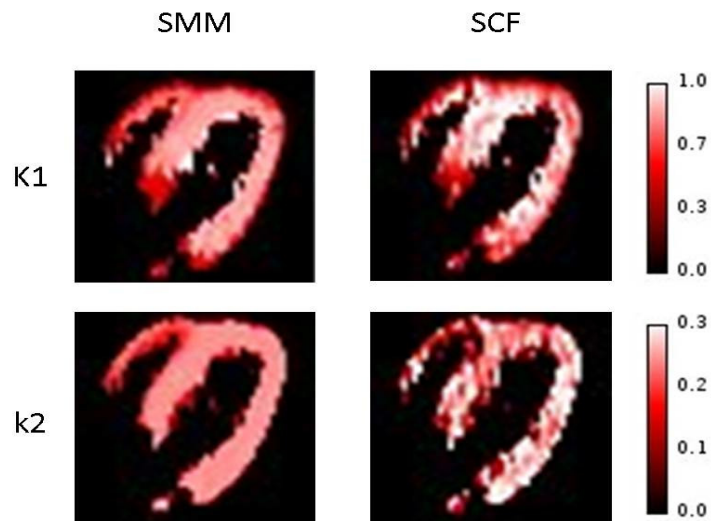


Figure 7: Parameter estimates for a single slice of the pig study data.